Microsc. Microanal. 22, 536–543, 2016
doi:10.1017/S1431927616000635

Microscopy AND Microanalysis

Improving Signal-to-Noise Ratio in Scanning Transmission Electron Microscopy Energy-Dispersive X-Ray (STEM-EDX) Spectrum Images Using Single-Atomic-Column Cross-Correlation Averaging

Jong Seok Jeong,* and K. Andre Mkhoyan*

Department of Chemical Engineering and Materials Science, University of Minnesota, Minneapolis, MN 55455, USA

Abstract: Acquiring an atomic-resolution compositional map of crystalline specimens has become routine practice, thus opening possibilities for extracting subatomic information from such maps. A key challenge for achieving subatomic precision is the improvement of signal-to-noise ratio (SNR) of compositional maps. Here, we report a simple and reliable solution for achieving high-SNR energy-dispersive X-ray (EDX) spectroscopy spectrum images for individual atomic columns. The method is based on standard cross-correlation aided by averaging of single-column EDX maps with modifications in the reference image. It produces EDX maps with minimal specimen drift, beam drift, and scan distortions. Step-by-step procedures to determine a self-consistent reference map with a discussion on the reliability, stability, and limitations of the method are presented here.

Key words: STEM-EDX, cross-correlation, subatomic precision, averaging, image processing

Introduction

With recent advances in analytical scanning transmission electron microscopy (STEM), including use of aberration correction of the lenses and high-efficiency electron energy-loss (EEL) and energy-dispersive X-ray (EDX) spectrometers, it has become routine practice to obtain atomic-resolution compositional maps of crystalline specimens (Bosman et al., 2007; Kimoto et al., 2007; Muller et al., 2008; Chu et al., 2010; D'Alfonso et al., 2010; Kotula et al., 2012; Suenaga et al., 2012; Jiang et al., 2013). To further improve signal-to-noise ratio (SNR) for these compositional maps, which are now limited by specimen damage, it is common practice to take several individual maps, or several sections from a single map, and to average them using a standard cross-correlation algorithm (Frank et al., 1978; Saxton & Baumeister, 1982). Frank et al. (1978) applied this approach to average electron micrographs of individual molecules with a radial pattern. The approach is particularly valuable for materials that are very sensitive to electron beam damage, resulting in low-dose or short-exposure images. Although this approach is an acceptable solution for most cases, to achieve a relatively high SNR in EELS or EDX maps, and thus to perform quantitative analysis for subunit cell or individual atomic-column information with unprecedented details, further improvement in data treatment is needed. Yankovich et al. (2014) recently demonstrated that, in case of annular dark-field (ADF) STEM images, sub-pm precision measurement for the positions of atoms could be achieved by applying nonrigid registration during cross-correlation and averaging of a series of short-exposure images. This approach might also work for compositional maps, if the SNR of raw maps is high enough. However, it should be noted that EELS or EDX maps often have very low SNR compared with ADF images [less than ~7 orders of magnitude, when high-collection-angle quad-Si(Li) windowless detectors are used] (Harrach et al., 2009). Here, we report a simple, reliable, and step-by-step solution to achieve high-SNR two-dimensional (2D) EDX spectrum images for individual atomic columns of crystalline specimens from standard STEM-EDX map data.

Received December 3, 2015; accepted February 29, 2016
*Corresponding authors. mkhoyan@umn.edu (KAM), jsjeong@umn.edu (JSJ)

Materials and Methods

Materials and STEM Specimen Preparation

For this study, undoped $SrTiO_3$ samples were tested. Electron-transparent STEM specimens were prepared using focused ion beam (FIB) lift-out (FEI Quanta 200 3D, FEI Company, Hillsboro, OR, USA), which was conducted using a 30 kV Ga ion beam followed by a 5 kV Ga ion beam to minimize Ga ion-damaged layers. The thickness of specimens was determined using the EELS log-ratio method (Egerton, 2011) with a mean free path for bulk plasmon generation (for 300 keV electrons) in $SrTiO_3$ of $\lambda_p = 123$ nm (LeBeau et al., 2008). The range of specimen thickness was 34–58 nm.

STEM Operational Conditions

An aberration-corrected (CEOS DCOR probe corrector) FEI Titan G2 60-300 STEM equipped with a Schottky X-FEG gun monochromator (FEI Company, Hillsboro, OR, USA) was used in this study. The microscope was operated at

300 keV. A carbon diffraction grating replica coated with Au nanocrystals was used for aberration correction. Once high-angle ADF (HAADF) imaging resolution was achieved within a range of 0.7–0.8 Å, the $SrTiO_3$ specimen was inserted. High-resolution HAADF-STEM images of the $SrTiO_3$ specimens were also acquired immediately before starting EDX experiments with acquisition parameters such as: beam current (50 pA), convergent semiangle (24.5 mrad), detector collection angle (50–200 mrad), dwell time (2–6 μs/pixel), and scan area ($2{,}048 \times 2{,}048$ pixel^2).

STEM-EDX maps were obtained using the FEI Super-X system, a quad-silicon drift windowless in-polepiece EDX detector, enabling efficient X-ray collection with higher X-ray count rates than standard Si(Li) detectors (Harrach et al., 2010). Microscope conditions were kept the same as for HAADF-STEM imaging; only the beam current was increased to 150 pA using monochromator focus optics for higher EDX signal. For each 256×256 pixel^2 EDX map acquired with a dwell time of 3 μs/pixel, we selected an area 32×32 Å^2 in size (about 8×8 $SrTiO_3$ unit cells) without any defects or unusual contrast. Frame by frame drift correction using the Bruker Esprit 1.9 software was performed to improve the spatial precision of EDX acquisitions. Overall, acquisition time for every experiment was in the range of 190–240 s, depending on the level of spatial specimen drift.

Results and Discussion

Extraction of X-Ray Counts from Each Elemental Peak

Figure 1 shows a cumulative EDX spectrum formed by summing up all spectra in a 256×256 map of a $SrTiO_3$ sample to show all X-ray peak positions and relative intensities. Strong peaks from Sr, Ti, and O are visible, as are several minor peaks (most notably Cu from the support washer and transmission electron microscopy holder, and Ga from ion implantation during FIB milling). Sr Kα, Sr L, and Ti Kα peaks are not overlapped with each other or peaks from other elements, allowing straightforward processing; however, Ti L and O K peaks have some overlap with each other. To extract net X-ray counts from each peak, all peaks were selected with proper energy windows (as presented in Table 1) and the net X-ray counts from the elemental peak of interest were extracted using algorithms

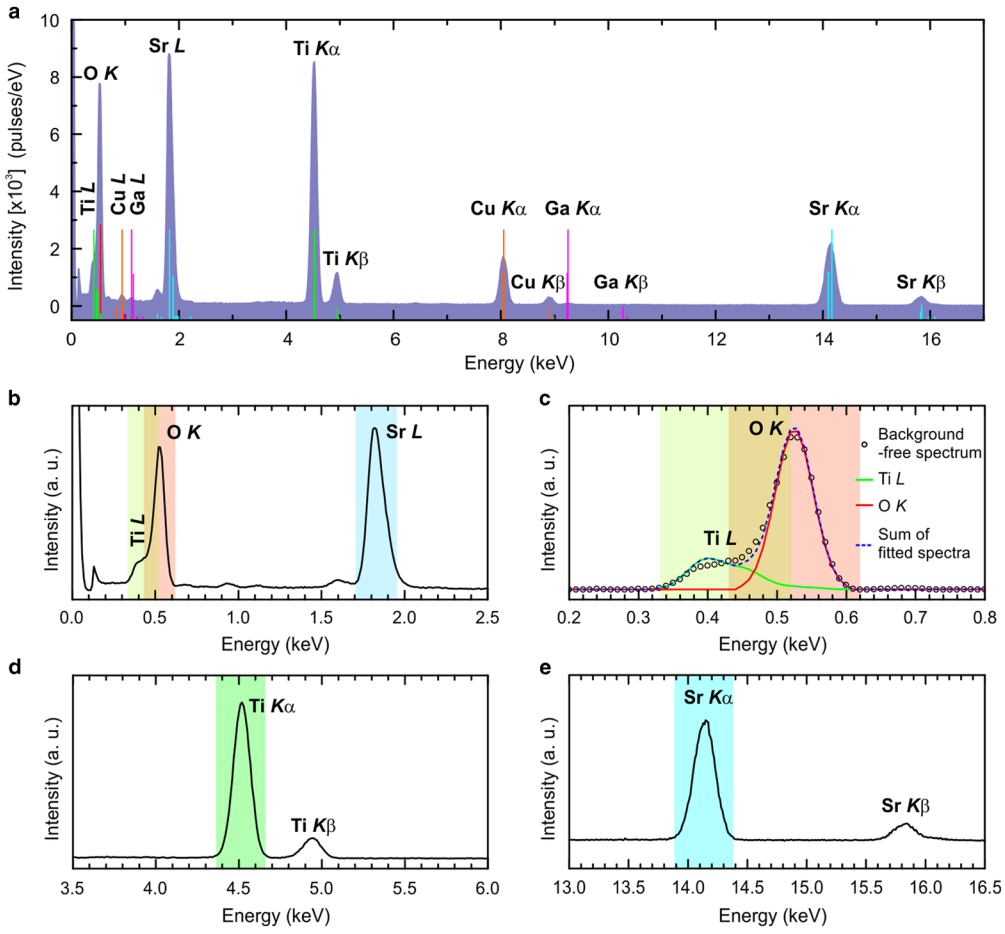

Figure 1. a: A cumulative energy-dispersive X-ray (EDX) spectrum formed from an EDX map of a $SrTiO_3$ sample. Strong peaks from Sr, Ti, and O, as well as minor peaks from Ga and Cu, are shown. Energy windows for EDX elemental maps are displayed in (**b–e**). Overlapped Ti L and O K peaks were resolved as shown in (**c**).

Table 1. X-Ray Peak Positions, Integration Energy Windows, and Net X-Ray Counts from Each Elemental Peak for an Energy-Dispersive X-Ray Mapping Experiment.

	Sr Kα	Sr L	Ti Kα	Ti L	O K
Peak position (keV)	14.14	1.82	4.51	0.42	0.52
Energy window size (keV)	0.50	0.23	0.31	0.19	0.19
Energy range of the window (keV)	13.89–14.39	1.71–1.94	4.36–4.67	0.33–0.52	0.43–0.62
Portion of peak area (%)	99	99	99	99	99
Net X-ray counts (pulses) from data in Figure 1	0.49×10^6	1.08×10^6	1.09×10^6	0.16×10^6	0.54×10^6

implemented in the Bruker Esprit 1.9 software. The procedure is as follows: elements of interest are selected, the Bremsstrahlung background is subtracted, each peak is fitted, and then the net X-ray counts from peaks in the windows are presented as corresponding elemental maps. This procedure is conducted pixel by pixel to produce the maps. As for Ti L and O K, the peaks were resolved first by series Bayes deconvolution implemented in the Bruker Esprit 1.9 software, as demonstrated in Figure 1c, before calculating the integrated intensity. As can be seen from Figure 1 and Table 1, the net X-ray counts of Ti L signal is considerably weaker than the Sr Kα, Sr L, and Ti Kα signals, which results in a lower SNR map.

For the EDX maps a 256×256 pixel^2 area from each X-ray peak was interpolated to 600×600 pixel^2 size using a bilinear interpolation routine (Press et al., 2007) for subsequent image processing. As the minimum shift in the cross-correlation is limited by pixel size, the interpolation of original maps is needed to reduce the pixel size by increasing the number of pixels in the maps, thus allowing more accurate alignment of the maps with a finer shift. It should be noted that specifics of the interpolation is not critical here. For example, bilinear and bicubic interpolations produce practically indistinguishable outcomes in final averaged maps (not presented here). Figure 2 shows an example of processed EDX elemental maps of Sr Kα, Sr L, Ti Kα, Ti L, and O K peaks from the $SrTiO_3$ sample. The EDX maps in Figure 2 were produced by standard cross-correlation averaging using maps including multiple atomic columns: the interpolated EDX maps were cut into four equal-sized individual images and then cross-correlated with each other and averaged. The maps of Sr Kα, Sr L, and Ti Kα, which have stronger EDX peak intensities, show acceptable SNR to identify positions of the atoms, but it could be further improved to retrieve detailed subunit cell (atomic-column) information in the maps.

Improving SNR in EDX Maps

Cross-Correlation

To improve the SNR of the acquired STEM-EDX maps, EDX signals in each atomic column were averaged using a standard cross-correlation. The method only includes lateral shifts between images with no rotation. The step-by-step procedure can be described as following:

Step 1. STEM-EDX maps consisting of around 8×8 $SrTiO_3$ unit cells (the number of unit cells varies according to the scan area selected) are cut into individual single-column images that include a single atomic column with an extra "buffer" region (5.35×5.35 Å^2, 101×101 pixel^2). The extra buffer region (about 20%) is used to accommodate the lateral shifts because cross-correlation inevitably produces artifacts at the boarders.

Two advantages of this step are as follows: (i) it allows obtaining many images to average from a relatively small area of the map with minor or no variation of thicknesses between them, and (ii) the individual images are cut to a size of about a unit cell and, therefore, are relatively free from common issues associated with specimen drift, beam drift, or scan distortion (Sang & LeBeau, 2014). The areas selected in a raw Sr L EDX map are shown in Figure 3a. In this example

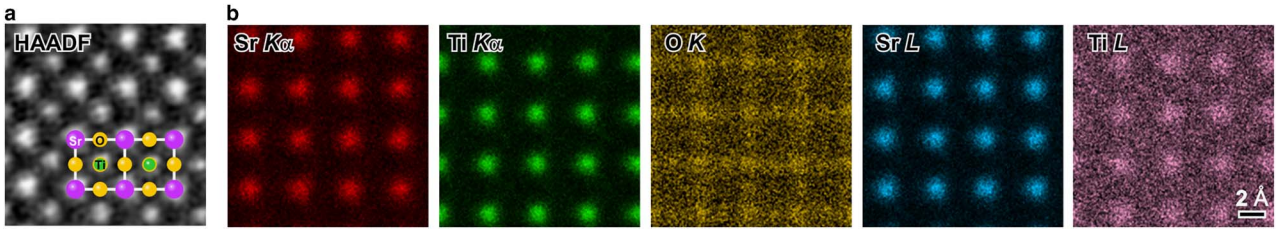

Figure 2. a: Typical high-angle annular dark-field (HAADF) scanning transmission electron microscopy (STEM) image of $SrTiO_3$ viewed along the [001] crystallographic direction with a model of the atomic positions overlaid showing locations and composition of the atomic columns. The HAADF image was low-pass filtered to limit signals <0.65 Å. **b:** Multicolumn cross-correlation averaged STEM energy-dispersive X-ray elemental maps of Sr Kα/L, Ti Kα/L, and O K peaks from a $SrTiO_3$ sample. All maps are normalized to span the maximum and minimum intensities of each image.

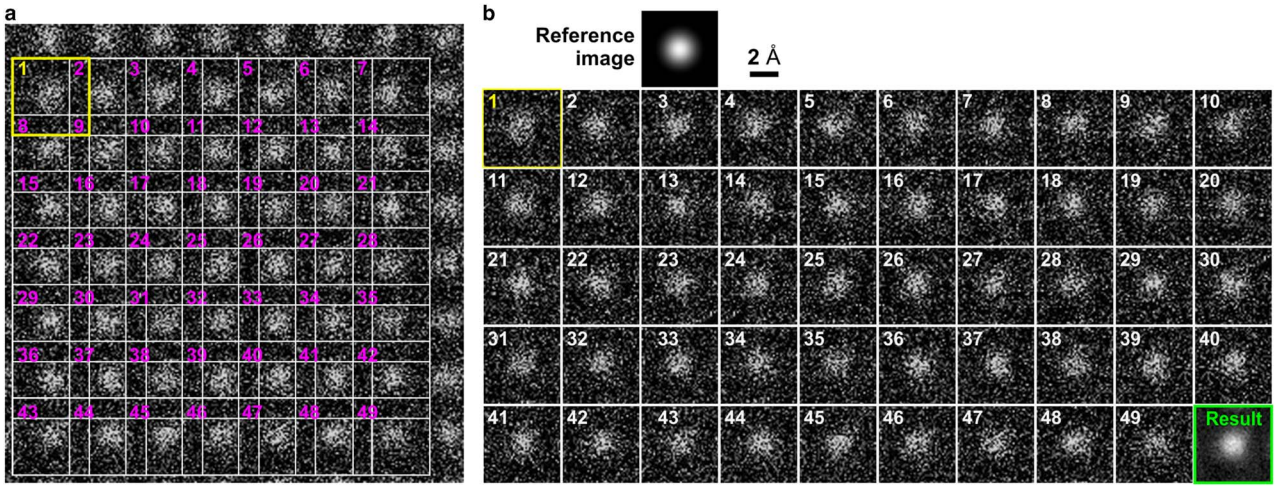

Figure 3. a: An interpolated Sr L energy-dispersive X-ray map of 600×600 pixel^2 image size, where 49 overlapping squares 101×101 pixel^2 in size are selected with each approximately centered on a Sr atomic column. **b:** In all, 49 individual single-column images from (**a**). A reference image, two-dimensional Gaussian with a full-width at half-maximum of 1.48 Å, was used to align the 49 images by applying a cross-correlation algorithm and then the images were averaged into a resulting final image (labeled as "Result").

49 individual images are cut from Figure 3a (Fig. 3b). The number of single-column images cut from raw EDX maps can vary according to the scan area selected. In this report it was in the range of 40–60 images. The main window for the cut should be $a \times a$, where a is the spacing between identical columns of interest, which is the same as the unit cell size here. To add a buffer region, we found it is safe to extend the size of the window up to about 20%. Even though the bigger window is preferable to minimize artifacts, too large of a buffer area should be avoided because the signals from neighboring columns will start to influence the cross-correlation.

Step 2. Determining a reference image. Selection of the reference image is critical. The next section will discuss two different methods for unbiased determination of this reference image.

Step 3. The individual single-column images are aligned to the reference image using the standard cross-correlation algorithm (Frank et al., 1978; Saxton & Baumeister, 1982) and then averaged. As individual images are relatively noisy, none of these images can be used as a reliable reference (the cross-correlation algorithm is not stable for this level of noise).

Although any smooth 2D function (2D Gaussian, 2D Lorentzian, etc.) with the same intensity scale, similar shape, and correct size will work, we used a 2D Gaussian image as the reference image to demonstrate the steps. Using a circularly symmetric reference image removes possible shape biasing of the final averaged EDX map. Figure 3b shows the reference image and the resulting image ("Result" in Fig. 3b) after these steps.

Determination of a 2D Reference Image

The size of the 2D Gaussian reference image plays a critical role in the cross-correlation process. To determine unbiasedly the proper size of the 2D Gaussian reference image, two different approaches with consistent results, could be used.

For the first approach, experimental images are cross-correlated to two different 2D Gaussian images, one known to be too narrow and another known to be too wide [in this case, full-width at half-maximum (FWHM) of 0.8 and 2.0 Å for narrow and wide, respectively], and then the resulting cross-correlated image is used as the new reference image for the next iteration. After two to three cycles of iterative cross-correlation, the measured FWHM of the cross-correlated images converge to stable values: 1.39 Å for Sr Kα, 1.48 Å for Sr L, and 1.35 Å for Ti Kα (Fig. 4).

A second approach for selecting the proper size for a 2D reference image relies on determination of a curve representing the FWHM of the resulting image as a function of the one used for the reference image:

Step 1. A set of 2D Gaussian reference images is generated with sizes gradually varying from one known to be too narrow to another known to be too wide (in this case, FWHMs from 0.5 to 4.0 Å).

Step 2. Experimental images are cross-correlated to this set of 2D Gaussian reference images with various FWHMs and are averaged.

Step 3. The FWHM of the averaged images resulting from Step 2 is plotted as a function of the FWHM of the Gaussian reference images used and the intersection of this curve with the $y = x$ line would determine the correct size of the 2D Gaussian reference.

To show the reliability of this approach, we demonstrated it on artificially constructed EDX maps with various noise levels. 2D Gaussian images with a FWHM of 1.40 Å were created to simulate the experimental Sr Kα map (see Fig. 5a). Specifically, a set of 500 artificial 2D Gaussian images with a

FWHM of 1.40 Å are created. The center of each Gaussian function is randomly offset within the range of ±5 pixels from the frame center for further cross-correlation. Then, Gaussian noise (while any noise will work for this purposes, we choose Gaussian noise for simplicity) with 0 mean and variance (v) ranging from 0 to 0.5 is applied to each set of 2D Gaussian images to model noisy experimental data (see Fig. 5a). The sets of simulated noisy EDX maps are cross-correlated to 2D Gaussian reference images with a FWHM in the range 0.5–4.0 Å and are averaged. The FWHM of each resulting cross-correlation averaged image is then measured. The results are presented in Figure 5b.

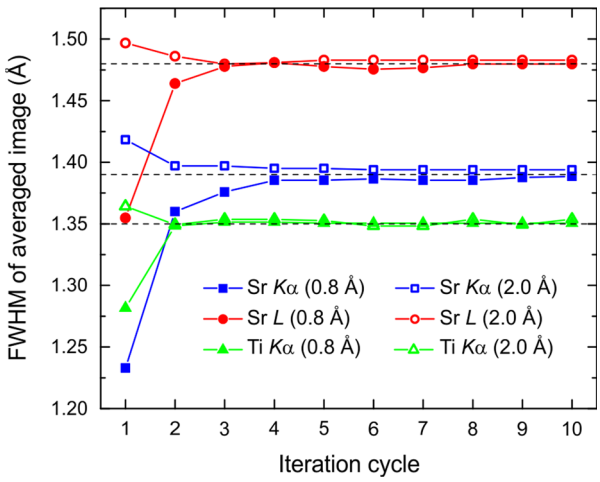

Figure 4. Iteration of cross-correlation process of experimental energy-dispersive X-ray (EDX) maps to determine a proper size for reference image. The first cycle of cross-correlations was performed using a two-dimensional Gaussian image with full-width at half-maximum (FHWM) of 0.8 Å (solid) and 2.0 Å (open). The subsequent outcomes of each iteration were used as the reference images for the next iteration. Converged values are indicated qby the dotted lines for each case: Ti Kα (1.35 Å), Sr Kα (1.39 Å), and Sr L (1.48 Å). We consider that the slight divergence in the Sr Kα case is due to local minimum of the cross-correlation process resulting from noise in the maps.

As the FHWM of the reference image increases, the one in the resulting cross-correlation averaged image increases. This means that if the size of the 2D Gaussian reference image is chosen improperly, it can either increase (in the case of an oversized reference) or decrease (in the case of an undersized reference) the size of the final cross-correlation averaged image; and the higher the noise level, the greater is the deviation from the actual object size due to a mis-sized reference (noise degrades the proper alignment of images to the reference). In these simulations, we could expect the measured FWHM of the averaged image to have the same FWHM as the reference image used ($y = x$ in Figure 5). As shown in Figure 5b, the measured FWHM of the averaged images has a crossover at the $y = x$ line. The method provides a robust solution for the FWHM, which is practically independent on a noise level of the individual maps. Therefore, for an actual experimental data set, the proper size of the reference image can be determined from the intersection with a curve from the experimental data and the $y = x$ line. The FWHM values of reference images for the experimental data set, as shown in Figure 6, are found to be

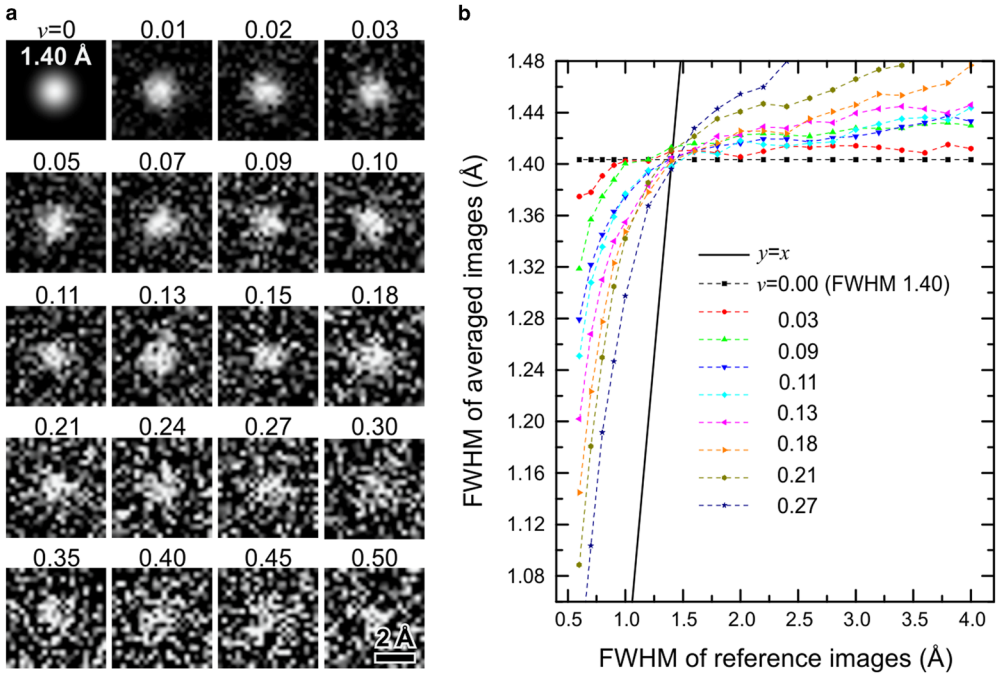

Figure 5. **a:** Gaussian noise with 0 mean and different variances (v) was added to the two-dimensional Gaussian image with a full-width at half-maximum (FWHM) of 1.40 Å. **b:** The FWHM of averaged images as a function of the FWHM of reference images was used. The line following the $y = x$ function is presented in the plot, indicating the self-consistent FWHM determination point.

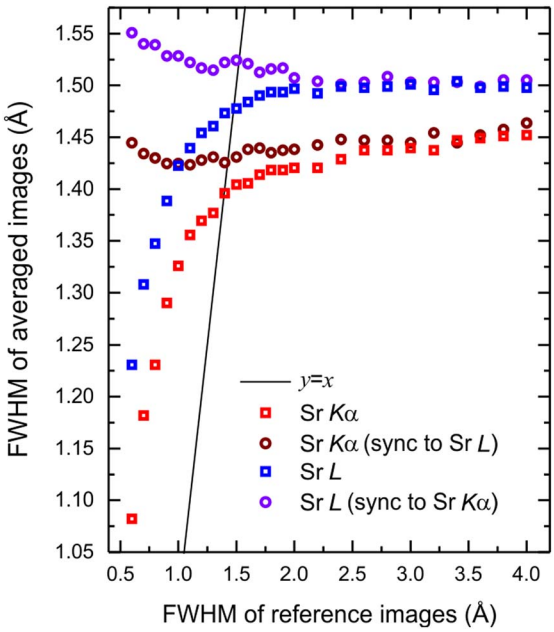

Figure 6. The full-width at half-maximum (FWHM) of averaged experimental energy-dispersive X-ray Sr maps as a function of the FWHM of reference images used. The image shifts in the cross-correlation of Sr Kα are synchronized to those of Sr L, and vice versa. The line following the $y = x$ function is presented in the plot, indicating the self-consistent FWHM determination point.

1.39 Å for Sr Kα and 1.48 Å for Sr L, which are in excellent agreement with that derived using the first approach.

In addition, it is natural to think that when two different EDX maps are formed using different X-ray peaks, which are emitted from the same atomic column, EDX maps with lower SNR can be spatially synchronized to the cross-correlation of the maps with higher SNR (or EDX maps to HAADF images acquired in parallel). It should be noted that X-ray emission and signal delocalization are center-symmetric relative to the atomic column, as they all originate from the center-symmetric atomic orbitals. All EDX maps from the same atomic column are also center-symmetric and centered to the column. Therefore, the shifts obtained from one map can be used without limitation as those for the other maps. We tested reliability of the synchronization of one EDX map to another. When single-column Sr Kα image sets are cross-correlated and averaged, the same shifts were applied to each corresponding Sr L image (referred to here as "synchronization"). This means that the cross-correlation alignment applied for each single-column Sr Kα image set is also applied to the corresponding Sr L image set. The results are presented in Figure 6. For completeness of the analysis, we also did the reverse: this time synchronizing the Sr Kα image set to the cross-correlated Sr L image set. As can be seen from Figure 6, the synchronization produces acceptable results with reasonable FWHM values for the resulting averaged EDX images. However, it also introduces a slight size increase in the averaged map when it is synchronized to the other map. The discrepancy appears to mainly originate from the noise in the primary maps. When the reference image is in the range smaller than the object, the cross-correlation algorithm tries to identify and align smaller features in the maps to the reference. These smaller features are noise dominated in the range. Therefore, when the secondary map is synchronized to the primary map, the noise in the secondary map is not efficiently canceled out, resulting in extra broadening of the secondary map. On the other hand, when the reference image is in the range larger than the object, the reference image defines the overall shape of the cross-correlated and averaged map, which in turn creates an inaccurate object in the synchronized secondary map. However, in this range, the synchronization process is less influenced by noise in the maps so that the size of the synchronized secondary map converges to that of the primary map. This noise-driven discrepancy will eventually disappear if the primary map has significantly low noise level. Although an ADF image, obtained in parallel with the EDX maps, appears to be suitable for the primary image, it can also introduce further complications due to ADF intensities from both Sr and Ti/O columns close enough to overlap. In EDX maps the overlap between neighboring column signals can be easily ignored, as they are considerably far apart.

Peak SNR (PSNR) Determination

PSNR (Sangwine & Horne, 1998) was employed to evaluate the level of SNR improvement with our cross-correlation averaging. The PSNR of the image with 0–1 intensity scale is defined as $-10\log_{10}MSE$, where MSE is the mean square error of the processed image relative to the original image. In this case, the MSE of the averaged images ("processed images") was estimated relative to the noise-free 2D Gaussian image ("original image"), which was used as a reference for the cross-correlation. It should be noted that the "processed" images are experimental data whereas the "original" image is simulated, and therefore PSNR comparison is qualitative. Figure 7 shows the evaluated PSNR as a function of the number of images averaged. The PSNR shows a rapid increase up to 30–70 maps of averaging for all three cases—Sr Kα, Sr L, and Ti Kα—and then slowly increases afterward. The transition point between the rapid and slow increase in the PSNR shifts toward the lower number for the EDX data with higher SNR. The level of PSNR, which can be reached in multicolumn cross-correlation averaging, such as ones shown in Figure 2, was indicated by the shaded area in Figure 7. Interestingly, it is noted that a small difference in the SNR of raw maps can result in a considerable difference in the number of maps required to reach the same level of PSNR, as is the case for Sr L and Ti Kα maps here (Table 1).

SNR-Improved Experimental EDX Maps

Figure 8 shows one of the examples for SNR-improved experimental EDX maps. Using the procedure described above, first the 2D Gaussian reference images for each map were determined and then SNR-improved Sr Kα/L and

Ti Kα/L EDX maps were produced (Fig. 8). During experiments, several sets of EDX maps were acquired. Each set of EDX maps produces SNR-improved Sr Kα/L and Ti Kα/L maps (Figs. 8a–8i), and then they are further cross-correlated to each other to produce the final result for that experiment ("Final" in Fig. 8). The final Sr and Ti maps in Figure 8 were produced by averaging 466 and 434 individual images, respectively. It is clearly seen that the SNR was dramatically improved in the final averaged maps. As shown in Figures 8a to 8i, the Ti L peak has relatively lower X-ray counts compared with other peaks (Table 1). Therefore, it has a higher noise level as compared with Sr Kα/L and Ti Kα peaks even after the SNR-improving steps. Note that here the cross-correlation of Ti L maps were synchronized to that of Ti Kα maps.

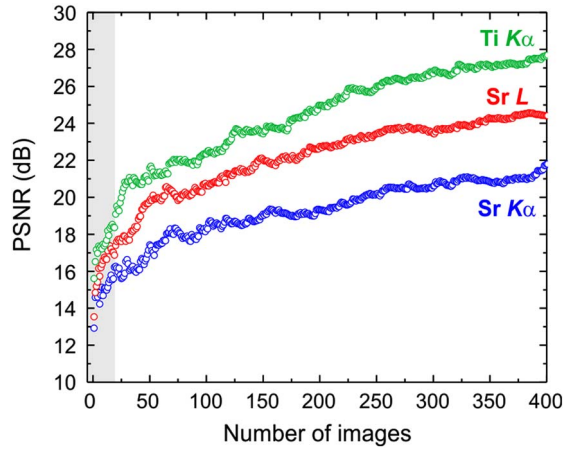

Figure 7. Peak signal-to-noise ratio (PSNR) as a function of the number of single-atomic-column energy-dispersive X-ray (EDX) images averaged. This data set corresponds to the one that was used to produce signal-to-noise ratio-improved single-atomic-column EDX maps, shown in Figure 9. The shaded area represents the PSNR level that can be achieved when the same data set is used for the multicolumn cross-correlation averaging, shown in Figure 2.

Finally, two different pairs of SNR-improved EDX maps from Sr and Ti are compared, and their radially averaged intensity profiles are also presented in Figure 9. As can be seen in Figure 9, such treatment of the data results in single-column EDX maps with sufficiently high SNR so that small differences in sizes between maps from K and L shells of each atomic column can be resolved. These maps, which now have considerably high SNR due to averaging of many individual maps, can be further analyzed for subunit cell information. For example, if effects of the channeling probe are properly removed, the excitation potentials can be extracted.

Conclusions

We demonstrated an improved and step-by-step cross-correlation averaging method that allows treatment of standard experimental STEM-EDX maps to achieve high-SNR 2D maps of atomic columns of crystalline specimens. The method is based on the use of a self-consistently determined reference map to cross-correlate many individual noisy maps that can be cut out from a few experimental STEM-EDX maps with relatively small scan area. The approach presented here may allow extraction of subtle physical information at the subunit cell or single atomic column level, such as delocalization of the EDX signals. The reliability and stability of the method are also tested. Although the method is demonstrated for an EDX data set, it can also be implemented without any modification for EELS maps. The method can also be coupled with other image-processing methods such as image filtering. We acknowledge that the residual scan distortions and drift, and other instrumentation noise influencing accuracy of the cross-correlation process are the next limiting factors in the precision of final SNR-improved single-atomic-column EDX maps. It should also be noted that the method relies on averaging of EDX signals from many atomic columns, and thus loses variation in compositions between individual atomic columns, if they exist.

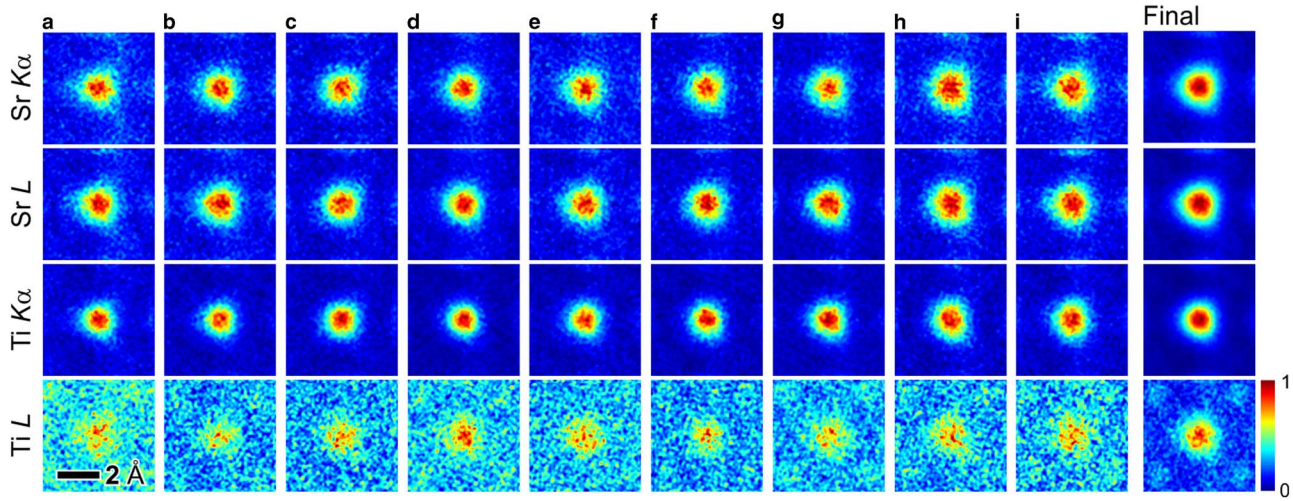

Figure 8. a–i: Signal-to-noise ratio (SNR)-improved single-atomic-column Sr Kα/L and Ti Kα/L energy-dispersive X-ray maps obtained from nine different runs of mapping. "Final" SNR-improved data from each peak of Sr and Ti are plotted. All images are rescaled to the standard 0 (minimum) to 1 (maximum) intensity range.

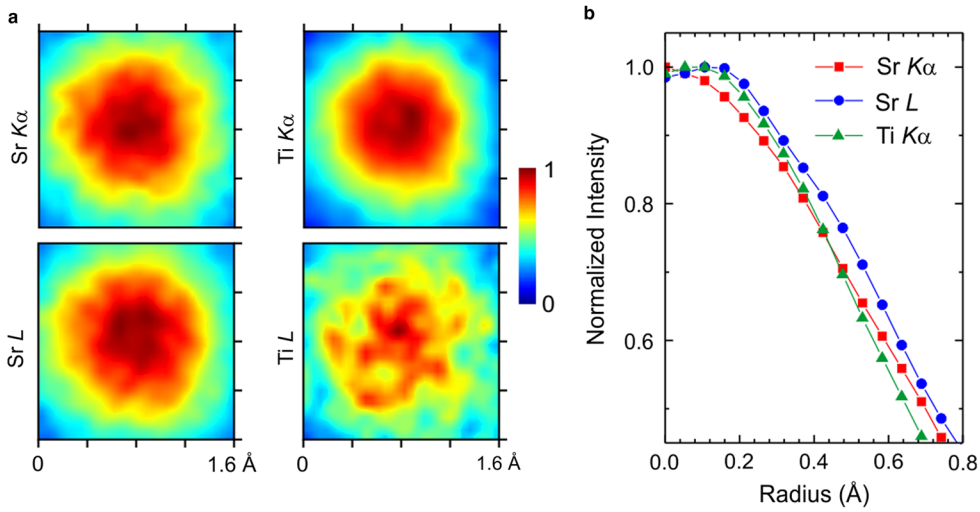

Figure 9. a: Magnified signal-to-noise ratio (SNR)-improved energy-dispersive X-ray maps from Sr Kα and L and Ti Kα and L peaks obtained from the "Final" in Figure 8 alongside their corresponding azimuthally averaged radial profiles in (**b**). The less circular shape of the Ti L map is due to much lower SNR in the data and the profile of the Ti L map was not included in (**b**) due to the insufficient SNR. The size difference between Sr Kα and Sr L is clearly visible.

Acknowledgments

This work was supported by the NSF MRSEC under award DMR-1420013. STEM analysis was carried out in the Characterization Facility of the University of Minnesota, which receives partial support from the NSF through the MRSEC program. The authors also thank Prashant Kumar for critically reading the manuscript.

References

Bosman, M., Keast, V.J., García-Muñoz, J.L., D'Alfonso, A.J., Findlay, S.D. & Allen, L.J. (2007). Two-dimensional mapping of chemical information at atomic resolution. *Phys Rev Lett* **99**, 086102.

Chu, M.W., Liou, S.C., Chang, C.P., Choa, F.S. & Chen, C.H. (2010). Emergent chemical mapping at atomic-column resolution by energy-dispersive X-ray spectroscopy in an aberration-corrected electron microscope. *Phys Rev Lett* **104**, 196101.

D'Alfonso, A.J., Freitag, B., Klenov, D. & Allen, L.J. (2010). Atomic-resolution chemical mapping using energy-dispersive x-ray spectroscopy. *Phys Rev B* **81**, 100101.

Egerton, R.F. (2011). *Electron Energy-Loss Spectroscopy in the Electron Microscope*. New York: Springer.

Frank, J., Goldfarb, W., Eisenberg, D. & Baker, T.S. (1978). Reconstruction of glutamine synthetase using computer averaging. *Ultramicroscopy* **3**, 283–290.

von Harrach, H.S., Dona, P., Freitag, B., Soltau, H., Niculae, A. & Rohde, M. (2009). An integrated silicon drift detector system for FEI Schottky field emission transmission electron microscopes. *Microsc Microanal* **15**, 208–209.

von Harrach, H.S., Dona, P., Freitag, B., Soltau, H., Niculae, A. & Rohde, M. (2010). An integrated multiple silicon drift detector system for transmission electron microscopes. *J Phys Conf Ser* **241**, 012015.

Jiang, Y., Wang, Y., Sagendorf, J., West, D., Kou, X., Wei, X., He, L., Wang, K.L., Zhang, S. & Zhang, Z. (2013). Direct atom-by-atom chemical identification of nanostructures and defects of topological insulators. *Nano Lett* **13**, 2851–2856.

Kimoto, K., Asaka, T., Nagai, T., Saito, M., Matsui, Y. & Ishizuka, K. (2007). Element-selective imaging of atomic columns in a crystal using STEM and EELS. *Nature* **450**, 702–704.

Kotula, P.G., Klenov, D.O. & von Harrach, H.S. (2012). Challenges to quantitative multivariate statistical analysis of atomic-resolution x-ray spectral. *Microsc Microanal* **18**, 691–698.

LeBeau, J.M., Findlay, S.D., Allen, L.J. & Stemmer, S. (2008). Quantitative atomic resolution scanning transmission electron microscopy. *Phys Rev Lett* **100**, 206101.

Muller, D.A., Kourkoutis, L.F., Murfitt, M., Song, J.H., Hwang, H.Y., Silcox, J., Dellby, N. & Krivanek, O.L. (2008). Atomic-scale chemical imaging of composition and bonding by aberration-corrected microscopy. *Science* **319**, 1073–1076.

Press, W.H., Teukolsky, S.A., Vetterling, W.T. & Flannery, B.P. (2007). *Numerical Recipes: The Art of Scientific Computing*. New York: Cambridge University Press.

Sang, X. & LeBeau, J.M. (2014). Revolving scanning transmission electron microscopy: Correcting sample drift distortion without prior knowledge. *Ultramicroscopy* **138**, 28–35.

Sangwine, S.J. & Horne, R.E.N. (1998). *The Colour Image Processing Handbook*. London: Chapman and Hall.

Saxton, W.O. & Baumeister, W. (1982). The correlation averaging of a regularly arranged bacterial cell envelope protein. *J Microsc* **127**, 127–138.

Suenaga, K., Okazaki, T., Okunishi, E. & Matsumura, S. (2012). Detection of photons emitted from single erbium atoms in energy-dispersive X-ray spectroscopy. *Nat Photonics* **6**, 545–548.

Yankovich, A.B., Berkels, B., Dahmen, W., Binev, P., Sanchez, S.I., Bradley, S.A., Li, A., Szlufarska, I. & Voyles, P.M. (2014). Picometre-precision analysis of scanning transmission electron microscopy images of platinum nanocatalysts. *Nat Commun* **5**, 4155.